

Effects of Simulated Particle Deposition on Film Cooling

S. A. Lawson

K. A. Thole

Department of Mechanical and Nuclear
Engineering,
Pennsylvania State University,
University Park, PA 16802

Diminishing natural gas resources has increased incentive to develop cleaner, more efficient combined-cycle power plants capable of burning alternative fuels such as coal-derived synthesis gas (syngas). Although syngas is typically filtered, particulate matter still exists in the hot gas path that has proven to be detrimental to the life of turbine components. Solid and molten particles deposit on film-cooled surfaces that can alter cooling dynamics and block cooling holes. To gain an understanding of the effects that particle deposits have on film cooling, a methodology was developed to simulate deposition in a low speed wind tunnel using a low melt wax, which can simulate solid and molten phases. A facility was constructed to simulate particle deposition on a flat plate with a row of film cooling holes. Infrared thermography was used to measure wall temperatures for quantifying spatially resolved adiabatic effectiveness values in the vicinity of the film cooling holes as deposition occurred. Results showed that deposition reduced cooling effectiveness by approximately 20% at momentum flux ratios of 0.23 and 0.5 and only 6% at a momentum flux ratio of 0.95. [DOI: 10.1115/1.4000571]

1 Introduction

The increasing demand for clean energy in a world with decreasing natural gas resources has focused recent attention on developing power generation turbines to operate alternative fuels such as coal-derived synthesis gas (syngas). Projects funded by the U.S. Department of Energy have set goals to achieve 45–50% efficiency and near-zero emissions from integrated gasification combined-cycle (IGCC) power plants by 2010 [1]. One of the major disadvantages of using alternative fuels is that they contain impurities that become entrained in the hot gas path of the turbine. Even with modern systems capable of filtering particles larger than $10 \mu\text{m}$, impurities from the fuels combined with impurities from the air can amount to 2 tons of ingested material in 8000 h of operation for a utility gas turbine [2]. Because of the high operating temperatures, pressures, and velocities that exist in gas turbines, the particulate matter deposits on turbine component surfaces. These turbine surfaces are highly dependent on sophisticated external cooling methods, such as film cooling, to prevent thermal fatigue. Deposition can increase surface roughness and in some cases block film cooling holes on first stage vane and endwall surfaces where cooling is most critical.

Little is known about the effects of particle deposition on turbine cooling because deposition is a complex process involving a three phase flow: solid and molten particles being convected by the hot gas exiting the combustor. In addition, the turbulent mixing between a coolant jet and the mainstream crossflow make deposition near film cooling holes a challenging process to predict. With a better understanding of deposition on cooling, new strategies can be developed to mitigate the negative effects of deposition on cooling.

The objective of the current study is to develop a method to simulate deposition and observe its effects on film cooling as it evolves. Infrared (IR) thermography was used to measure wall temperatures to characterize adiabatic effectiveness as particles deposited in the vicinity of a row of film cooling holes at various momentum flux ratios. This paper describes the methods associated with simulating gas turbine particle deposition in a low speed wind tunnel. A discussion of the adiabatic effectiveness results and their relationship with deposition will then be presented.

Contributed by the International Gas Turbine Institute (IGTI) of ASME for publication in the JOURNAL OF TURBOMACHINERY. Manuscript received July 20, 2009; final manuscript received July 20, 2009; published online October 21, 2010. Editor: David Wisler.

2 Review of Relevant Literature

After the oil embargo of 1973, interests were focused on developing alternative fuels for gas turbines. The foundation was laid for research related to deposition, erosion, and corrosion (DEC) in turbomachinery between the early 1970s and the early 1990s before the focus shifted toward optimizing natural gas fueled plants. Research conducted during this time period explored the dominant mechanisms of particle delivery to turbine surfaces that include inertial impaction, turbulent diffusion/eddy impaction, Brownian diffusion, and thermophoresis [3]. Dring et al. [4] conducted an analytical study to determine the nature of particle trajectories through turbine airfoils based on applied drag forces alone. They found that the trajectory of a particle is primarily dependent on the Stokes number, St_k , as defined in the nomenclature. Dring et al. [4] determined that particles having Stokes numbers less than 0.1 followed fluid streamlines, while particles with Stokes numbers greater than 10 impacted airfoil surfaces. In an earlier study, Friedlander and Johnstone [5] proposed that deposition involving particles with $St_k \ll 1$ is associated with eddy impaction because of turbulent diffusion in near wall regions.

Hamed et al. [3] utilized a particle delivery model to determine the relative rates of delivery for each of the dominant deposition mechanisms. The model showed that turbulent diffusion was the dominant delivery mechanism for particles smaller than $1 \mu\text{m}$ and was enhanced by eddy impaction as the particle size increased. As particle size increased further, inertial impaction became the dominant mechanism for delivery. Hamed et al. [3] found that, in general, delivery rate decreased as particle size decreased. Below $0.1 \mu\text{m}$, where Brownian diffusion is the dominant delivery mechanism, deposition rate remained constant.

Multiple studies have been conducted to explore the effects of gas temperatures and surface temperatures on particle deposition. Wenglarz and Fox [6], Walsh et al. [7], Richards et al. [8], and Wenglarz and Wright [9] all conducted studies relating deposition sticking mechanisms to gas and surface temperatures.

Wenglarz and Fox [6] conducted DEC experiments using coal-water fuels in a small scale turbine combustor. They observed that deposition rates increased with an increase in gas temperature. They attributed these increased deposition rates to the increased fraction of molten particulate that existed at elevated gas temperatures. Walsh et al. [7] studied the deposition of bituminous coal ash on a heat exchanger tube and observed the sticking process over time. They found that, initially, only molten particles would stick to the clean surface solidifying soon after deposition. As the

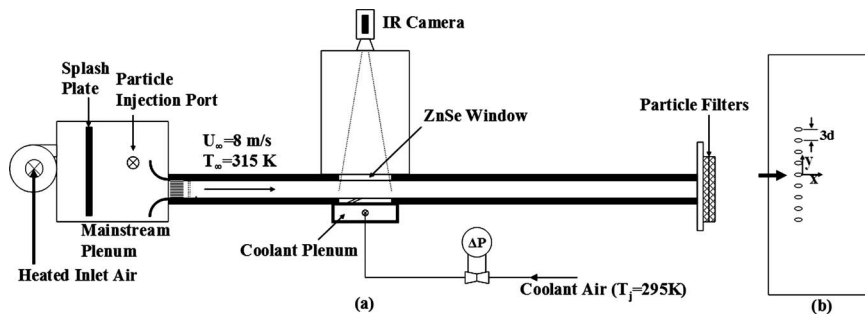


Fig. 1 Schematic of the (a) open loop wind tunnel and (b) film cooling endwall

thickness of the deposition increased, the temperature of the deposition surface exposed to the hot gases became hot enough that it remained sticky allowing both molten and solid particles to deposit. They found that, eventually, the rate that incoming particles deposited on the surface equaled the rate that particles detached because of erosion from incoming particles. Richards et al. [8] studied the deposition of bituminous coal ash in a reactor specifically designed to measure deposition at different gas and surface temperatures. They determined that a decrease in gas temperature increased ash particle size and resulted in increased sticking fraction. Richards et al. [8] also determined that increasing surface cooling decreased sticking fraction when particles were small enough to be sufficiently cooled by the thermal boundary layer prior to impaction. In their study, evaluating alternative fuels for gas turbines, Wenglarz and Wright [9] concluded that the gas temperature relative to the melting temperature of an entrained particulate was the relationship that best determined the sticking probability of particles that deposited by inertial impaction. This means that molten particles are more likely to stick to a surface than solid particles.

The idea of shifting to alternative fuels has led to numerous studies related to the effects of deposition on cooling effectiveness. Highlighted here are a few studies conducted to determine the effects of idealized deposits on endwall film cooling. Goldstein et al. [10] simulated roughness using cylindrical elements, which were sized and located based on turbine blade inspection. They measured a 10–20% decrease in wall effectiveness caused by roughness at low blowing ratios and a 40–50% improvement in effectiveness caused by roughness at high blowing ratios.

Bons et al. [11] measured surface roughness and generated detailed three-dimensional maps of in-service turbine components. They found that deposition created surfaces made up of random combinations of peaks, valleys, and plateaus. In regions downstream of film cooling holes, they observed a periodic distribution of furrows suggesting that coolant jets prevented deposition in the wakes of holes.

Cardwell et al. [12] and Sundaram et al. [13] simulated uniform roughness on a film-cooled endwall using sandpaper. Cardwell et al. [12] found that roughness caused a decrease in cooling effectiveness at high blowing ratios. They attributed the decreased effectiveness to coolant jet separation caused by a roughness induced thicker boundary layer. In a later study, Sundaram et al. [13] conducted a study to determine the effects of deposition on endwall film cooling near the leading edge of an inlet guide vane. In addition to the sandpaper, Sundaram et al. [13] manufactured deposits of ideal shapes and sizes based on measurements made by Bons et al. [11]. Sundaram et al. [13] found that when placed downstream of leading edge cooling holes, small deposits actually enhanced cooling effectiveness by 25% because of the jet interaction with the idealized deposit.

There have been few studies that have attempted to accomplish the task of actually simulating the process of particle deposition. Jensen et al. [14] operated the Turbine Accelerated Deposition Facility (TADF), which was designed to simulate deposition in an

accelerated manner. By increasing the concentration of particulate matter in the hot gas path, they could simulate 10,000 h of turbine operation in a 4 h test. The deposition simulation was carried out by injecting particles into a natural gas combustion process. The particle-laden exhaust gases impacted onto a removable coupon that could be analyzed following testing. The simulation methodology was validated using scanning electron microscope and x-ray spectroscopy analyses, which showed similarities to deposits found on actual turbine hardware.

Bons et al. [15] studied the evolution of deposition over time in the TADF by injecting particulate matter in different stages called “burns.” They measured the surface topology after every stage and recreated roughness models out of acrylic. Heat transfer coefficients were measured on each model to determine how deposition affected heat transfer as it evolved. They observed an initial increase in Stanton number after the first burn. Stanton number then leveled off through the third burn before increasing again after the fourth burn. Crosby et al. [16] studied the independent effects of particle size, gas temperature, and surface temperature on deposition in the TADF. They found that deposition rate increased with an increase in particle size, an increase in gas temperature, and an increase in surface temperature.

Ai et al. [17] conducted a study using the TADF to investigate the effects of deposition on a film-cooled coupon. The coupon was oriented such that particle-laden exhaust flow impacted the surface at a 45 deg angle simulating deposition by inertial impaction. In addition to measuring surface coverage, they measured surface temperatures using an RGB camera and were able to conclude that increased deposit height resulted in increased surface temperatures. By observing deposition behavior over time, they concluded that increased surface temperatures accelerated deposition resulting in a nonlinear deposit growth rate with time. They also observed the effects of film cooling blowing ratio on deposition growth and surface temperature. They concluded that an increase in blowing ratio resulted in a decrease in surface temperatures, which reduced deposition in coolant wakes.

The studies described above revealed much about the deposition process; however, there has never been a study versatile enough to both simulate the deposition process and closely observe the deposition process in the vicinity of film cooling holes. The goal of the present study is to simulate the deposition process in a way that allows for a close observation of the interaction between particle-laden flow and a film-cooled endwall.

3 Experimental Methods

Deposition simulations and film cooling effectiveness tests were conducted in a low speed open loop wind tunnel shown in Fig. 1. Room air was heated by space heaters at the suction side of the blower at the inlet to the plenum. Upon entering the plenum, the heated air impinged onto a splash plate, which prevented the air from propagating through to the tunnel without mixing.

The flow developed in a duct with a height of 6.9 cm (10.8d), a width of 41.7 cm (65.6d), and a hydraulic diameter of 11.8 cm

($18.6d$). A row of nine film cooling holes with an $L/d=3$, $P/d=3$, and $\alpha=30$ deg was drilled in a removable endwall plate. Placed $130d$ ($7D_h$) upstream of the holes at the tunnel entrance was a rounded inlet, a section of honeycomb, a double layer of screens, and a 2 mm trip wire. The endwall plate was constructed from a 2.5 cm thick low thermal conductivity polyvinyl foam block ($k=0.025$ W/m K) that minimized conduction losses to create an adiabatic wall condition. The surface of the film cooling plate exposed to the flow was covered by a thin layer of black contact paper. The contact paper provided a smooth surface that was easily replaceable between test cases. The mainstream flow continued $15D_h$ ($279d$) downstream from the film cooling plate before exiting through two particle filters. Laser Doppler velocimetry and particle image velocimetry were both used to measure turbulence intensity, T_u , with and without the honeycomb and screens installed. The freestream turbulence intensity was 4.6% with the honeycomb and screens installed and 12.3% without the honeycomb and screens. All baseline and deposition tests were conducted at high freestream turbulence ($T_u=12.3\%$), while only the baseline that provided a benchmark was completed at low freestream turbulence.

3.1 Adiabatic Effectiveness Measurements. Adiabatic effectiveness was quantified by heating the mainstream air to approximately 315 K and injecting coolant air at approximately 295 K. The mainstream velocity was set at 8 m/s, while the coolant flow was manually controlled to set the momentum flux ratio for a given test. Compressed air was used as the coolant and was routed through a plenum located beneath the film cooling plate as seen in Fig. 1. The coolant volumetric flowrate was measured using a laminar flow element (LFE).

A FLIR P20 IR camera was used to acquire a temperature map over the entire film-cooled endwall. Compared with conventional methods in which measurements could only be acquired where thermocouples were located, the spatially resolved technique used in this study allowed for adiabatic effectiveness to be calculated with $875 \mu\text{m}$ resolution everywhere on the film-cooled surface. A removable zinc selenide (ZnSe) window served as the top wall located above the film cooling plate. This ZnSe window allowed for maximum transmission to the IR camera, which was mounted above the test section in a box to minimize radiation from the surroundings. A series of five IR images was taken upon reaching a steady state condition for each test. Three calibration thermocouples were located on the surface of the film cooling plate in locations having different temperatures to cover the entire range measured by the IR camera for a given test. With the use of FLIR systems software, image calibration was performed by adjusting the background temperature and emissivity to match image temperature values with corresponding thermocouple measurements.

3.2 Uncertainty Analysis and Validation. An uncertainty analysis was performed for the momentum flux ratio, blowing ratio, and adiabatic effectiveness measurements using the method described by Moffat [18]. The blowing ratio uncertainty was calculated as ± 0.015 (3.13%), while the momentum flux ratio uncertainty was calculated as ± 0.010 (4.42%). The maximum bias and precision uncertainties of the wall temperatures measured by the IR camera were $\pm 0.528^\circ\text{C}$ and $\pm 0.222^\circ\text{C}$, respectively. Uncer-

Table 1 Uncertainty values

Variable	Bias	Precision	Uncertainty	%
M	-	-	± 0.015	3.13
I	-	-	± 0.010	4.42
η	-	-	± 0.037 at 0.3	-
	-	-	± 0.04 at 0.9	-
T_∞	0.500	0.154	$\pm 0.523^\circ\text{C}$	-
T_j	0.500	0.154	$\pm 0.523^\circ\text{C}$	-
T_w	0.528	0.222	$\pm 0.573^\circ\text{C}$	-

tainties in adiabatic effectiveness were calculated as ± 0.037 at an η value of 0.3 and ± 0.040 at an η value of 0.9. Uncertainties of major parameters and associated temperature bias and precision values are presented in Table 1.

To validate the measurement technique, adiabatic effectiveness for a single row of cylindrical film cooling holes was measured at $T_u=4.6\%$ and $T_u=12.3\%$. Figure 2 shows the centerline effectiveness plotted with respect to dimensionless downstream distance for a row of cooling holes having a momentum flux ratio of $I=0.23$. The $T_u=4.6\%$ case was measured to compare with literature data and the $T_u=12.3\%$ case was measured as a baseline for deposition studies. Both cases are shown in Fig. 2. Note that the measurements in Fig. 2 were made on an endwall without deposition. Table 2 shows the test conditions for the literature results used for comparison in Fig. 2. For the present cases, centerline effectiveness increases with a decrease in freestream turbulence. The $T_u=4.6\%$ case converges with most of the literature between $4d$ and $12d$ downstream of the cooling row, while the $T_u=12.3\%$ case falls below most of the literature and is in agreement with the data by Kunze et al. [19]. The range of data that could be acquired was limited to $12d$ downstream of the cooling holes because of visual access for IR measurement.

Figure 3 shows the laterally averaged effectiveness with respect to dimensionless downstream distance compared with the results from the literature. In contrast to the centerline data, the laterally averaged effectiveness decreases with a decrease in freestream

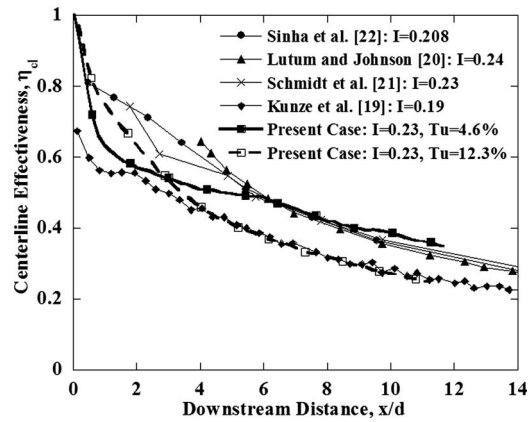


Fig. 2 Centerline effectiveness for $I=0.23$ with no deposition

Table 2 Comparison of film cooling conditions

Study	L/d	P/d	α (deg)	I	M	VR	DR	Tu (%)
Sinha et al. [22]	1.8	3.0	35	0.21	0.50	0.42	1.20	0.2
Schmidt et al. [21]	4.0	3.0	35	0.23	0.60	0.38	1.60	0.2
Lutum and Johnson [20]	3.5	2.9	35	0.24	0.52	0.45	1.15	3.5
Kunze et al. [19]	4.6	4.0	35	0.19	0.50	0.36	1.37	1.5
Present case	3.0	3.0	30	0.23	0.49	0.47	1.06	4.6/12.3

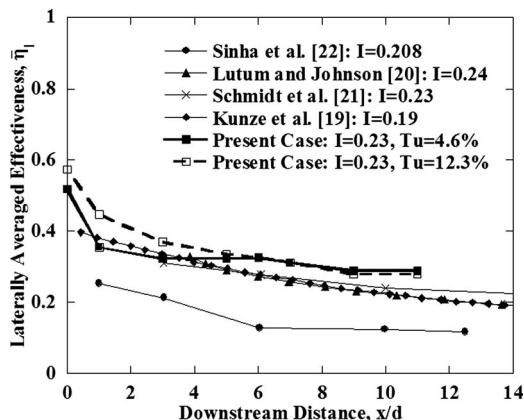


Fig. 3 Laterally averaged effectiveness for $I=0.23$ with no deposition

turbulence. The $Tu=4.6\%$ results agree reasonably well with Lutum and Johnson [20], Schmidt et al. [21], and Kunze et al. [19], but are higher than the results obtained by Sinha et al. [22]. Lutum and Johnson [20] studied the effect of cooling hole L/d on adiabatic effectiveness and found that effectiveness generally decreased with decreasing L/d . This is a probable reason for why the laterally averaged results by Sinha et al. [22] are lower than the rest of the benchmark data. Differences between the benchmark case at $Tu=4.6\%$ and the data from the literature exist possibly because of the difference in freestream turbulence levels measured between the present case and the studies in the literature. High freestream turbulence levels could enhance mixing between the jet and the mainstream and therefore increase lateral spreading of the coolant.

3.3 Deposition Simulation and Analysis. The objective of the current study was to develop a methodology that could be used in a laboratory setting to simulate deposition using a low speed wind tunnel. The method was developed so that adiabatic effectiveness tests could be conducted on a surface of interest following the deposition simulation. It was necessary to inject particles into a hot gas path that could simulate the deposition of both solid and molten materials. It is important to note that all deposition tests were conducted at high freestream turbulence ($Tu=12.3\%$), which was necessary to simulate the turbulence levels exiting a gas turbine combustor. Prior to the film cooling studies, various types of particles were injected into a flow with a cylindrical obstacle to observe the deposition behavior. Initially, sand was injected to simulate the deposition of solid particulate. Then, multiple waxes having different melting temperatures were injected to observe their deposition behavior. For the initial tests, red dye was added to the wax to make deposition easier to observe. Photos of sand deposition and wax deposition are shown in Fig. 4. Both materials deposited in a manner that illustrated the horseshoe vortex and saddle point locations on the endwall. The photos in Fig. 4 show examples of large particle deposition by

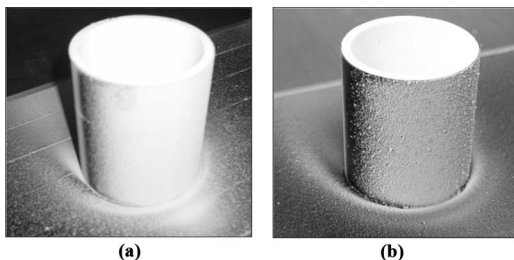


Fig. 4 Photographs of (a) sand deposition and (b) wax deposition on a cylinder

Table 3 Stokes number conditions

	Engine conditions	Simulation conditions
Gas temperature, T_∞ (K)	1590	315
Compressor pressure ratio, PR	16	-
Particle density, ρ_p (kg/m ³)	1980	900
Gas velocity, $U_\infty = U_p$ (m/s)	501	8
Gas viscosity, μ (kg/m s)	5.549×10^{-5}	1.852×10^{-5}
Chord, b (cm)	21.8	-
Chord/hole diameter, b/d	129	-
Hole diameter, $d=L_c$ (cm)	0.169	0.635

References [1,2,13,23].

inertial impaction on the cylinder and small particle deposition by turbulent diffusion and eddy impaction on the endwall. Ultimately wax was chosen to simulate both solid and molten particles under the assumption that only the largest particles would be in molten form upon reaching the deposition test surface. Calculations were performed to determine the distance a particle could travel before solidification [23]. For a particle with a given melting temperature and latent heat of fusion, solidification time was directly dependent on the initial wax temperature and the mainstream temperature, and particle size. Based on the achievable test conditions in the low speed wind tunnel, wax having a melting temperature of 328 K was chosen as the material for injection.

To simulate particle trajectories, it was necessary to match the wax Stokes number range to the Stokes number range that exists in actual engine conditions [23]. Table 3 shows the engine conditions and the simulation conditions used for the current study to calculate Stokes numbers. Figure 5 shows the wax particle size necessary to match Stokes number for a given engine particle size. The wax particle diameter required to match the engine condition Stokes number is approximately 13 times the diameter of a coal ash particle in actual engine conditions.

The wax particle size distribution in the low speed wind tunnel was measured using a Malvern Spraytec particle analyzer capable of characterizing aerosol droplets in the size range 0.1–2000 μm . Figure 6 shows the size distribution and corresponding Stokes numbers for the wax particles in the low speed wind tunnel facility. Recall from Fig. 5 that a 130 μm wax particle in simulation conditions is scaled by Stokes number to match the trajectory of a 10 μm coal ash particle in engine conditions. In Fig. 6, there is a vertical line at 130 μm which intersects the % mass passing curve at approximately 90% (as shown on the secondary y-axis) indicating that approximately 90% (by mass) of the wax particles are smaller than 130 μm in diameter.

Figure 7 indicates temperatures of wax particles that are and are

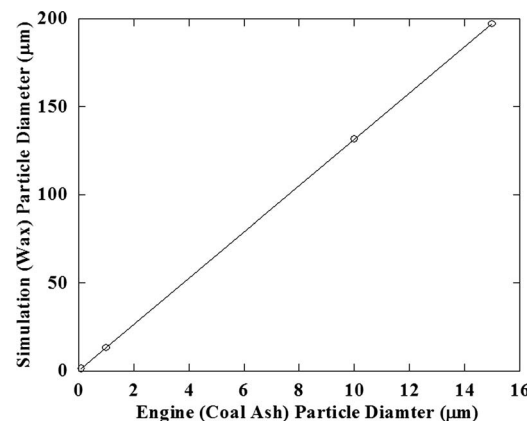


Fig. 5 Wax particle diameter required to match engine condition Stokes number

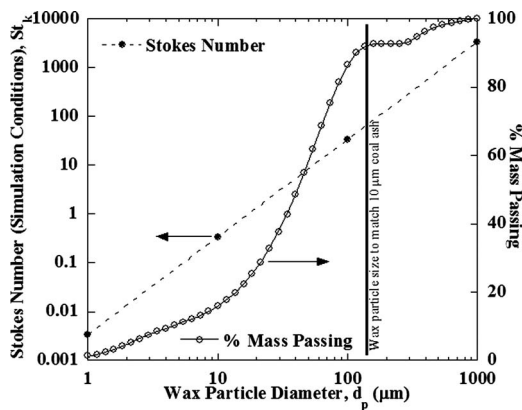


Fig. 6 Wax particle size distribution and corresponding Stokes number in lab simulation conditions

not exposed to the film cooling jet relative to convective distance for a 13 μm particle and a 130 μm particle. The particle temperature relationship to travel distance was calculated using a simple lumped mass approximation. Initially, all particles are in molten form and are losing heat to the mainstream while they cool. The heat loss rate is shown by

$$\dot{Q} = hA_p(T_p - T_\infty) \quad (1)$$

By assuming the particle moves at the same velocity as the mainstream, the heat transfer coefficient can be calculated from the analytic solution for conduction from a sphere [24]. The particle temperature as a function of time is shown by

$$T_p = (T_{p,i} - T_\infty)e^{(-hA_p/\rho_p C_p V_p)t} + T_\infty \quad (2)$$

When the temperature of a given particle reaches the material solidification temperature, the phase change process begins. During the phase change process, the particle continues to lose heat to the surroundings; however, the particle remains at the solidification temperature of the material. The time that the phase change process takes to complete is calculated using

$$t_s = \frac{\Delta H_{\text{fus}}}{\dot{Q}} \quad (3)$$

When the particle is exposed to the film coolant, the governing equations remain unchanged; however, the temperature of the surroundings changes to the coolant temperature.

As seen in Fig. 7, the 13 μm particle cools faster than the

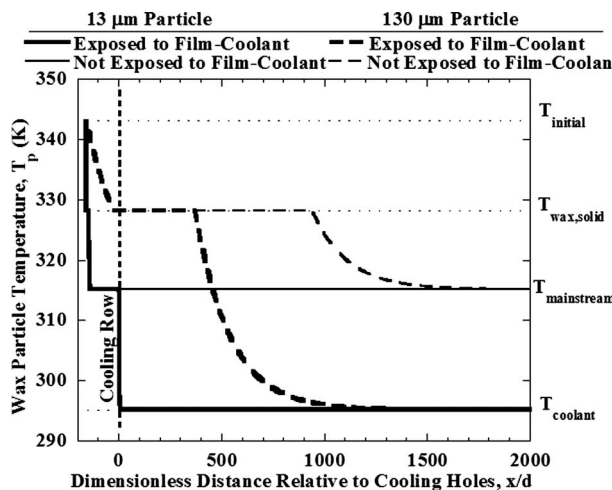


Fig. 7 Wax particle temperature relative to travel distance

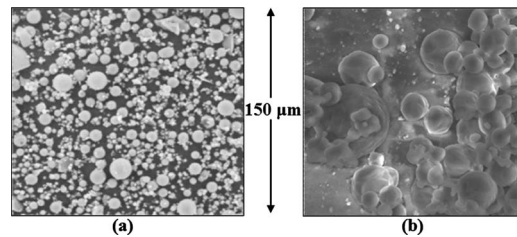


Fig. 8 ESEM images of (a) coal ash [2] and (b) wax particles

130 μm particle and is at the same temperature as the mainstream upon reaching the film cooling row. When the 13 μm solid particle enters the coolant, the particle temperature quickly drops to the coolant temperature further reducing its chances of depositing. The 130 μm particle does not solidify prior to reaching the coolant jets and is in the process of solidifying when it becomes entrained in the coolant flow. The coolant does increase the rate of heat loss from the particle but does not reduce the particle temperature until the phase change process has completed. When exposed to the coolant gases, the 130 μm particle would be in solid form 370 d downstream of the cooling row. If the 130 μm particle was not exposed to the coolant flow, it would not solidify until it reached a distance of 940 d downstream of the cooling row. Because the 130 μm particle is in molten form upon reaching the cooling row, it has a greater chance of depositing just downstream of the coolant holes than the 13 μm particle.

Figure 8 shows photographs of coal ash [2] and wax deposits taken using an environmental scanning electron microscope (ESEM). The photos show that wax deposits are spherical like the coal ash particles but are much larger.

Deposition tests were carried out by injecting molten wax particles using a spray gun especially designed for high viscosity fluids. The spray gun was attached to the particle injection port located on the side of the mainstream plenum downstream of the splash plate. A resistance heater was used to heat the wax reservoir that was instrumented with a thermocouple to control the initial wax temperature prior to injection. For each test case, 400 g of wax was injected eight times. The initial temperature of the molten wax was set so that particles greater than 50 μm in diameter would remain in molten form for a distance of 100 cm allowing them to reach the film-cooled endwall. After each injection cycle, a series of IR images of the film-cooled endwall was taken and calibrated using the method described in Sec. 2. Initial tests indicated that during deposition there were no significant changes to the emissivity of the surface, which verified the typical calibration procedure for a surface with deposits.

In addition to acquiring IR images, digital photographs were taken between each injection cycle. Digital photos were taken using a Nikon D40x 10.2 megapixel camera that was mounted in the same way as the IR camera. Surface lighting was provided by two fluorescent lamps mounted at opposing angles. To reduce surface glare, a polarizing filter was used with the Nikon D40x. The digital photographs were postprocessed using IMAGEJ software to determine the endwall area fraction covered by wax deposits after each injection.

Figure 9 illustrates the postprocessing procedure to capture the deposit sizes starting with an image of the surface without deposition and an image of the surface with deposition. For the post-processing, each digital image is converted to an 8 bit image to which each pixel is assigned a gray value between 0 and 255 corresponding to its brightness. After an image is converted to 8 bit, it can be treated as a two-dimensional matrix. The background is then subtracted by taking the difference between an image of the surface with deposition and an image of the surface without deposition. The resulting image showing only pixels representing deposition is then converted to a binary image. Conversion to binary is accomplished by setting pixels with low gray

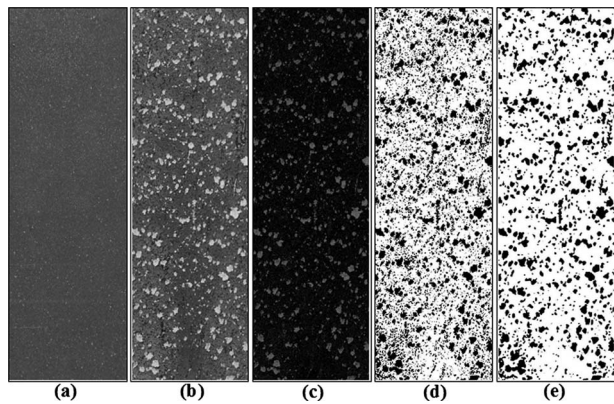


Fig. 9 Photographs illustrating the surface (a) without deposition, (b) with deposition, (c) after background subtraction, (d) after binary conversion, and (e) after median filter

values to 0 and pixels with high gray values to 1 resulting in a black and white picture in which black pixels represent deposits. At this point, it is necessary to remove any background noise that was not eliminated by the initial background subtraction. To do this, a median filter is used, which effectively removes any pixel grouping that is smaller than a user-defined pixel value. Then, the deposition area fraction is represented by the ratio of black to white pixels.

4 Discussion of Results

In their study evaluating the independent effects of density ratio, blowing ratio, and momentum flux ratio on film cooling, Thole et al. [25] concluded that a coolant jet will either remain attached, separate and reattach, or separate and remain detached from the endwall depending on momentum flux ratio. In the present study, adiabatic effectiveness tests were conducted at momentum flux ratios of $I=0.23$, $I=0.5$, and $I=0.95$ to observe the effects of deposition for the three different regimes described by

Table 4 Test conditions for deposition tests

I	M	VR	DR	Tu (%)
0.23	0.49	0.47	1.06	12.3
0.50	0.73	0.69	1.07	12.3
0.95	1.01	0.95	1.07	12.3

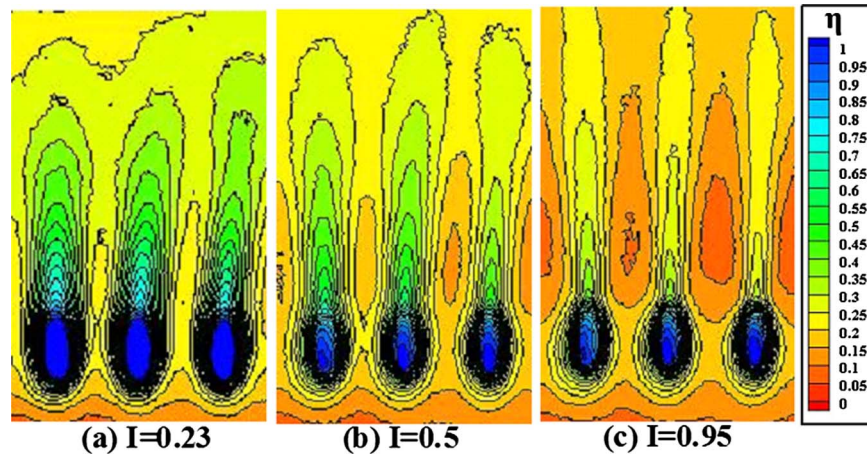


Fig. 10 Effectiveness contour plots at momentum flux ratios of (a) 0.23, (b) 0.5, and (c) 0.95

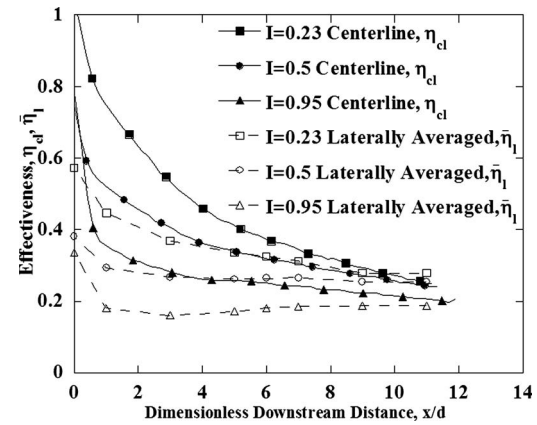


Fig. 11 Centerline and laterally averaged effectiveness plotted with respect to dimensionless downstream distance for all momentum flux ratios

Thole et al. [25]. Table 4 shows the conditions for each adiabatic effectiveness test conducted for the deposition study.

Figure 10 shows the contour plots of adiabatic effectiveness for each momentum flux ratio tested prior to deposition. The contours illustrate the effectiveness characteristics of each flow regime. As the momentum flux ratio increases from 0.23 to 0.5, laterally averaged effectiveness decreases implying that separation may be occurring at $I=0.5$. When momentum flux ratio is increased to 0.95, the contours illustrate low effectiveness laterally and along the centerline implying that separation is occurring. Figure 11 shows centerline and laterally averaged effectiveness with respect to dimensionless downstream distance for all three momentum flux ratios. Figure 11 shows that centerline and laterally averaged effectiveness decreases with an increase in momentum flux ratio when separation occurs.

Figure 12 shows effectiveness contour plots and corresponding deposition photographs at $I=0.23$. The appearance of the deposition in each photograph depends on the state of a particle when it impacts the surface. The deposits caused by molten particles show up as black splats, while deposits caused by solid particles show up as white spots. For the initial injection, only molten particles appear to deposit on the surface. Eventually, molten deposition increases the surface roughness to a point that solid particulate begins to deposit. As more injections occur, solid and molten particles deposit and further increase surface roughness. Although endwall temperatures were measured after all eight injection

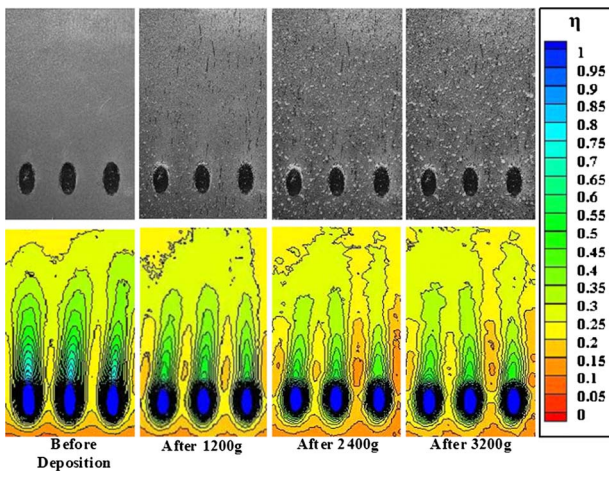


Fig. 12 Deposition development photographs and corresponding effectiveness contour plots at $I=0.23$

cycles, the effects of deposition are well represented by the data taken after 1200 g (3 cycles), after 2400 g (6 cycles), and after 3200 g (8 cycles), as seen in Fig. 12. Close inspection of each deposition photograph reveals that deposition concentration appears to be lower directly downstream of the film cooling holes, implying that the coolant jets themselves help prevent deposition. It can also be seen that solid particles build up over time inside the trailing edge of the film cooling holes.

Figure 13 shows the centerline effectiveness at $I=0.23$ after each wax injection cycle. Centerline effectiveness is affected by deposition after the first three to four injections shown and begins to reach a steady level between five and eight injection cycles. This pattern supports the observation made by Walsh et al. [7] that the deposition process eventually reaches an equilibrium state where the rate of deposition equals the rate that existing deposits are eroded by incoming particles that do not stick. Figure 14 shows the laterally averaged effectiveness after each wax injection cycle for $I=0.23$. As deposition increases, laterally averaged effectiveness decreases at all downstream locations but appears to have a greater impact on effectiveness in regions within $3d$ of the cooling hole trailing edge than in regions farther downstream.

The deposition development was quantified by counting deposits using IMAGEJ software. For a binary image, the software counts the pixel groupings and categorizes them based on area coverage. An equivalent deposit diameter was then calculated for each pixel grouping. Figure 15 shows a histogram of deposit size as it developed with increased injection for $I=0.23$. It is important to note

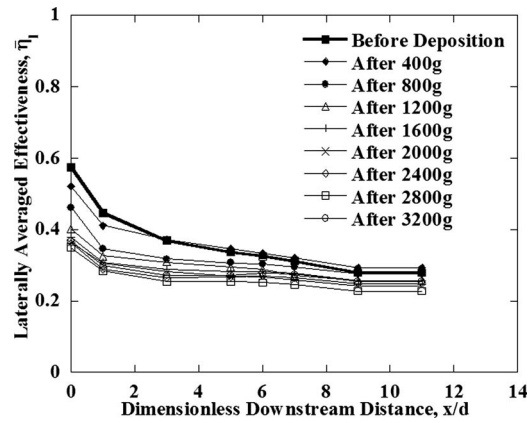


Fig. 14 Laterally averaged effectiveness development with deposition for $I=0.23$

that Fig. 15 does not show the histogram of particle sizes but rather deposit sizes. Each deposit could be made up of an agglomeration of many individual particles. The figure shows that as more wax is injected, both the size and number of deposits increase because of new particles adhering directly on the surface and onto existing deposits. The histograms indicate that the amount of deposit on the surface approaches an equilibrium state after eight injection cycles (3200 g). Histograms of deposit size for $I=0.5$ and $I=0.95$ showed a similar development trend as the histogram for $I=0.23$ implying that the time to reach a deposition equilibrium state is independent of momentum flux ratio.

Figure 16 shows the effectiveness contour plots and corresponding deposition photographs at $I=0.5$. The well defined wake region indicates that deposition is mitigated by the coolant jets immediately downstream of the film cooling holes. There also appears to be more deposition of solid particles at $I=0.5$ than at $I=0.23$, which could be caused by particles solidifying in the coolant layer prior to impacting the surface. This cooling effect would be enhanced by the higher coolant flow at $I=0.5$. The contour plots show that effectiveness decreases with an increase in deposition. From the contours, it is evident that deposition shortens the downstream influence of each coolant jet.

Figure 17 shows the effectiveness contour plots and corresponding deposition photographs for $I=0.95$. Similar to the two previous cases, the photographs show that deposition in regions near the cooling hole trailing edge are mitigated by the coolant jet itself. Deposition in these near wake regions is mitigated for two reasons. First, the coolant jets cool the large molten particles causing them to solidify prior to impacting the surface. Second, the

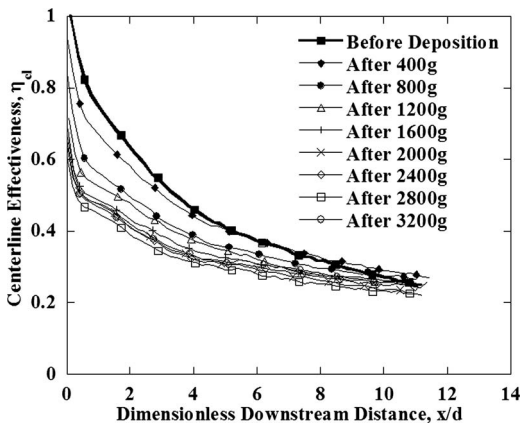


Fig. 13 Centerline effectiveness development with deposition for $I=0.23$

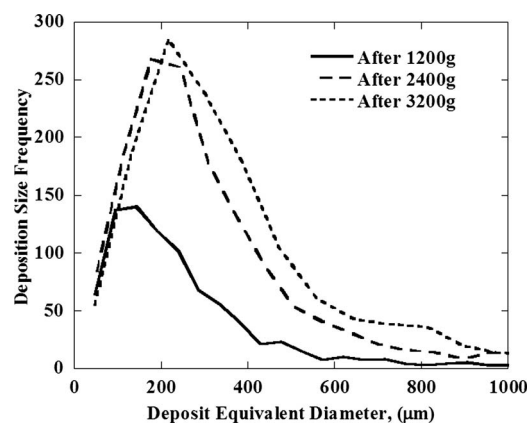


Fig. 15 Histograms of deposit sizes at different stages of deposition for $I=0.23$

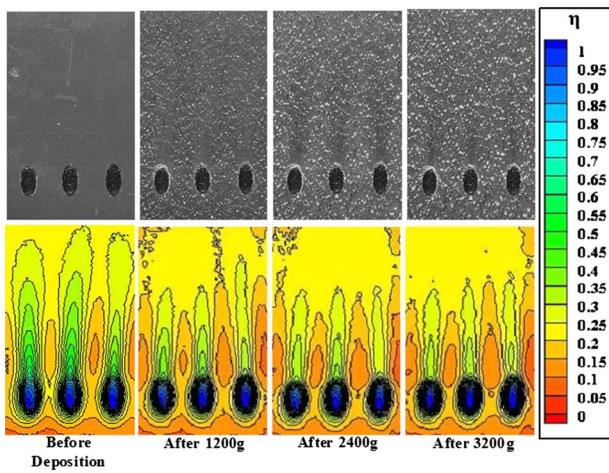


Fig. 16 Deposition development photographs and corresponding effectiveness contour plots at $I=0.5$

trajectories of the small solid particles are greatly influenced by the coolant jets preventing them from impacting the surface in near wake regions. The only particles that deposit in near wake regions are particles that are large enough to maintain their trajectories and withstand solidification by coolant jets.

Figure 17 shows that deposition has less of an effect on cooling at $I=0.95$ than it does at the lower momentum flux ratios. This lesser effect is because the jet separation at $I=0.95$ prevents high levels of adiabatic effectiveness downstream of the coolant holes even without deposition on the surface. Because of coolant jet separation at $I=0.95$, deposition has less of an effect at that momentum flux ratio than for $I=0.5$ or $I=0.23$. From the contours, the deposition enhances jet interaction, which ultimately improves lateral spreading of the coolant in far wake regions. The conduction effect of the wax is very small given it has a relatively low thermal conductivity ($k=0.24$ W/m K). Because the conduction effect can be neglected, the improved lateral spreading is attributed to the roughness created by large deposits in far wake regions rather than a conductive effect.

Figure 18 shows the area-averaged effectiveness reduction with respect to deposition area coverage. For $I=0.23$ and $I=0.5$, area-averaged effectiveness is reduced sharply through the first three injection cycles. For $I=0.23$ and $I=0.5$, the reduction in effectiveness approaches 20% as deposition area coverage increases. On the other hand, at $I=0.95$, the reduction in effectiveness reaches a

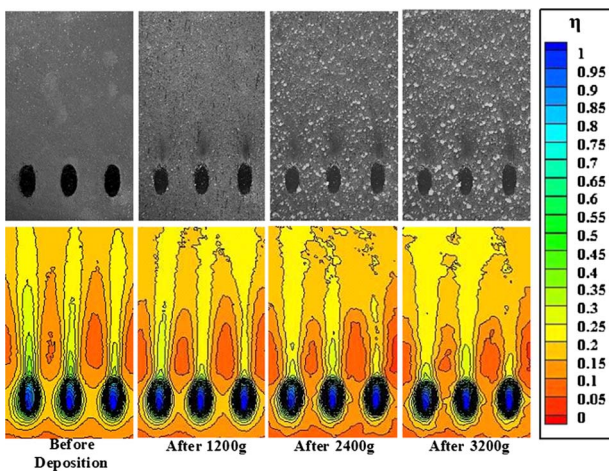


Fig. 17 Deposition development photographs and corresponding effectiveness contour plots at $I=0.95$

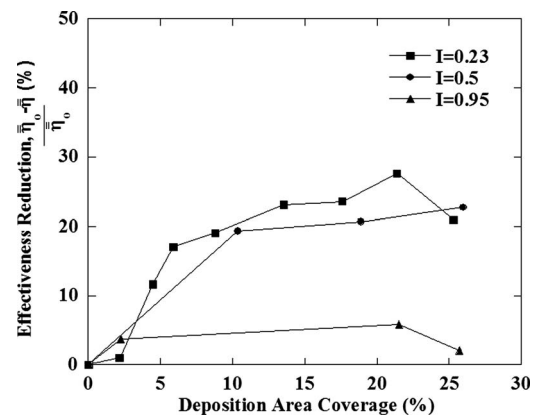


Fig. 18 Area-averaged effectiveness reduction with respect to deposition area coverage for all three momentum flux ratios

maximum of 6% before actually improving to 2% after the final injection cycle. The reduction in effectiveness was low at $I=0.95$ because the initial cooling provided by these separated jets was very low prior to deposition.

5 Conclusions

A methodology was determined to observe the effects of simulated deposition on film cooling through the use of a low melting temperature wax injectant. Cooling effectiveness was quantified by obtaining spatially resolved temperatures to calculate adiabatic effectiveness in the vicinity of a row of film cooling holes. The method for quantifying cooling effectiveness was validated by comparison with adiabatic effectiveness results from the literature.

Deposition was simulated by injecting molten wax particles into the mainstream. Simulation conditions were controlled so that the size range of injected wax particles scaled with Stokes number to the size range of coal ash particles in engine conditions. The present study focused on simulating deposition by inertial impaction and turbulent diffusion enhanced by eddy impaction.

Deposition was simulated for three different momentum flux ratios: $I=0.23$, $I=0.5$, and $I=0.95$ to observe the effects of deposition on cooling for three different jet conditions. For all momentum flux ratios, deposit coverage appeared to be less concentrated in near wake regions of each film cooling hole. Deposition in near wake regions was prevented because coolant jets solidified large particles and changed the trajectories of small particles preventing both from adhering to the surface. Large particles in molten form were the only particles found to have deposited in the near wake of the jets.

As deposition developed, the deposit sizes and total number of deposits increased implying that incoming particles adhered to the surface creating new deposits and to existing deposits increasing their size. Based on deposit size histograms and reductions in adiabatic effectiveness, the deposition process seemed to approach an equilibrium state after eight injection cycles. For $I=0.23$ and $I=0.5$, the effectiveness was reduced by 20% as deposition approached an equilibrium state. For $I=0.95$ effectiveness reached a maximum reduction of 6% and a final reduction after eight injection cycles of 2%. There was a different effect on cooling at $I=0.95$ because the coolant jets were separated from the surface prior to deposition, which inhibited cooling even without the existence of deposits. Because deposition had a similar effect on the reduction of cooling at $I=0.23$ and $I=0.5$, the results indicated no significant advantage of deposition on cooling for these flow regimes.

Acknowledgment

This publication was prepared with the support of the U.S. Department of Energy (DOE), Office of Fossil Fuel, and the National

Energy Technology Laboratory (NETL). The writers would like to specifically thank Jason Albert and Dr. David Bogard for their continued communication and support on the subject matter. This research was conducted under a subcontract that was sponsored by the U.S. DOE-NETL through a cooperative agreement with the South Carolina Institute for Energy Studies at Clemson University.

Nomenclature

A_p	= particle surface area
b	= chord length
C_p	= particle specific heat
ΔH_{fus}	= latent heat of fusion
ΔP	= pressure drop
d	= film cooling hole diameter, $d=0.635 \text{ cm}$
d_p	= particle diameter
D_h	= duct hydraulic diameter
DR	= density ratio, $DR=\rho_j/\rho_\infty$
h	= heat transfer coefficient
I	= momentum flux ratio, $I=\rho_j U_j^2 / \rho_\infty U_\infty^2$
L	= film cooling hole length
L_c	= characteristic length for Stokes number
M	= blowing ratio, $M=\rho_j U_j / \rho_\infty U_\infty$
P	= film cooling hole pitch
Q	= particle heat loss to surroundings
St	= Stanton number, $St=h/\rho C_p U$
St_k	= Stokes number, $St_k=\rho_p d_p^2 U_p / 18 \mu L_c$
t_s	= solidification time
T_j	= coolant jet temperature
T_p	= particle temperature
T_w	= wall temperature
T_∞	= mainstream temperature
Tu	= turbulence intensity percent, $Tu=u_{\text{rms}}/U_\infty$
U_j	= coolant jet velocity
U_p	= particle velocity
U_∞	= mainstream velocity
V_p	= particle volume
VR	= velocity ratio, $VR=U_j/U_\infty$
x	= streamwise distance from cooling hole trailing edge
y	= spanwise distance from center cooling hole

Greek

α	= film cooling hole incidence angle
η	= adiabatic effectiveness, $\eta=(T_\infty-T_w)/(T_\infty-T_j)$
η_{cl}	= centerline effectiveness
$\bar{\eta}$	= laterally averaged effectiveness
$\bar{\bar{\eta}}$	= area-averaged effectiveness
$\bar{\bar{\eta}}_0$	= baseline area-averaged effectiveness (no deposition)
ρ_j	= coolant jet density
ρ_p	= particle density
ρ_∞	= mainstream density
μ	= gas dynamic viscosity

References

- [1] Dennis, R.A., Shelton, W.W., and Le P., 2007, "Development of Baseline Performance Values for Turbines in Existing IGCC Applications," Paper No. GT2007-28096.
- [2] Bons, J. P., Crosby, J., Wammack, J. E., Bentley, B. I., and Fletcher, T. H., 2007, "High-Pressure Turbine Deposition in Land-Based Gas Turbines From Various Synfuels," ASME J. Eng. Gas Turbines Power, **129**, pp. 135–143.
- [3] Hamed, A., and Tabakoff, W., 2006, "Erosion and Deposition in Turbomachinery," J. Propul. Power, **22**(2), pp. 350–360.
- [4] Dring, R. P., Caspar, J. R., and Suo, M., 1979, "Particle Trajectories in Turbine Cascades," J. Energy, **3**(3), pp. 161–166.
- [5] Friedlander, S. K., and Johnstone, H. F., 1957, "Deposition of Suspended Particles From Turbulent Gas Streams," Ind. Eng. Chem., **49**, pp. 1151–1156.
- [6] Wenglarz, R. A., and Fox, R. G., 1990, "Physical Aspects of Deposition From Coal-Water Fuels Under Gas Turbine Conditions," ASME J. Eng. Gas Turbines Power, **112**, pp. 9–14.
- [7] Walsh, P. M., Sayre, A. N., Loehden, D. O., Monroe, L. S., Beer, J. M., and Sarofim, A. F., 1990, "Deposition of Bituminous Coal Ash on an Isolated Heat Exchanger Tube: Effects of Coal Properties on Deposit Growth," Prog. Energy Combust. Sci., **16**, pp. 327–345.
- [8] Richards, G. A., Logan, R. G., Meyer, C. T., and Anderson, R. J., 1992, "Ash Deposition at Coal-Fired Gas Turbine Conditions: Surface and Combustion Temperature Effects," ASME J. Eng. Gas Turbines Power, **114**, pp. 132–138.
- [9] Wenglarz, R. A., and Wright, I. G., 2003, "Alternate Fuels for Land-Based Turbines," *Proceedings of the Workshop on Materials and Practices to Improve Resistance to Fuel Derived Environmental Damage in Land-and Sea-Based Turbines*, Colorado School of Mines, Golden, Co., Oct. 22–24, pp. 4–45–4–64.
- [10] Goldstein, R. J., Eckert, E. R. G., Chiang, H. D., and Elovic, E., 1985, "Effect of Surface Roughness on Film Cooling Performance," ASME J. Eng. Gas Turbines Power, **107**, pp. 111–116.
- [11] Bons, J. P., Taylor, R. P., McClain, S. T., and Rivir, R. B., 2001, "The Many Faces of Turbine Surface Roughness," ASME J. Turbomach., **123**, pp. 739–748.
- [12] Cardwell, N.D., Sundaram, N., and Thole, K.A., 2005, "Effects of Mid-Passage Gap, Endwall Misalignment, and Roughness on Endwall Film-Cooling," Paper No. GT2005-68900.
- [13] Sundaram, N., and Thole, K.A., 2006, "Effects of Surface Deposition, Hole Blockage, and TBC Spallation on Vane Endwall Film-Cooling," Paper No. GT2006-90379.
- [14] Jensen, J. W., Squire, S. W., Bons, J. P., and Fletcher, T. H., 2005, "Simulated Land-Based Turbine Deposits Generated in an Accelerated Deposition Facility," ASME J. Turbomach., **127**, pp. 462–470.
- [15] Bons, J.P., Wammack, J.E., Crosby, J., Fletcher, D., and Fletcher, T.H., 2006, "Evolution of Surface Deposits on a High Pressure Turbine Blade, Part II: Convective Heat Transfer," Paper No. GT2006-91257.
- [16] Crosby, J.M., Lewis, S., Bons, J.P., Ai, W., and Fletcher, T.H., 2007, "Effects of Particle Size, Gas Temperature, and Metal Temperature on High Pressure Turbine Deposition in Land Based Gas Turbines From Various Synfuels," Paper No. GT2007-27531.
- [17] Ai, W., Murray, N., Fletcher, T. H., Harding, S., Lewis, S., and Bons, J. P., 2008, "Deposition Near Film Cooling Holes on a High Pressure Turbine Vane," Paper No. GT2008-50901.
- [18] Moffat, R. J., 1985, "Uncertainty Analysis in the Planning of an Experiment," ASME J. Fluids Eng., **107**, pp. 173–181.
- [19] Kunze, M., Preibisch, S., Vogeler, K., Landis, K., and Heselhaus, A., 2008, "A New Test Rig for Film Cooling Experiments on Turbine Endwalls," Paper No. GT2008-51096.
- [20] Lutum, E., and Johnson, B. V., 1999, "Influence of the Hole Length-to-Diameter Ratio on Film Cooling With Cylindrical Holes," ASME J. Turbomach., **121**, pp. 209–216.
- [21] Schmidt, D. L., Sen, B., and Bogard, D. G., 1996, "Film Cooling With Compound Angle Holes: Adiabatic Effectiveness," ASME J. Turbomach., **118**, pp. 807–813.
- [22] Sinha, A. K., Bogard, D. G., and Crawford, M. E., 1991, "Film-Cooling Effectiveness Downstream of a Single Row of Holes With Variable Density Ratio," ASME J. Turbomach., **113**, pp. 442–449.
- [23] Albert, J., 2008, personal communication.
- [24] Incropera, F. P., and DeWitt, D. P., 2002, *Fundamentals of Heat and Mass Transfer*, 5th ed., Wiley, New York.
- [25] Thole, K. A., Sinha, A. K., and Bogard, D. G., 1990, "Mean Temperature Measurements of Jets with a Crossflow for Gas Turbine Film Cooling Application," *Rotating Transport Phenomena*, J. H. Kim and W. J. Yang, eds., Hemisphere, New York.